J Mater Sci (2019) 54:8892–8906

Chemical routes to materials

Synergistic adsorption and visible-light catalytic degradation of RhB from recyclable 3D mesoporous graphitic carbon nitride/reduced graphene oxide aerogels

Ce Xu[1,2], Jin Wang[1,2,*], Boru Gao[1,2], Mengmeng Dou[1,2], and Rui Chen[1,2]

[1] *Department of Municipal and Environmental Engineering, Beijing Jiaotong University, Haidian District, Beijing 100044, China*
[2] *Beijing Key Laboratory of Aqueous Typical Pollutants Control and Water Quality Safeguard, Beijing 100044, China*

Received: 19 December 2018
Accepted: 12 March 2019
Published online: 19 March 2019

ABSTRACT

In this work, a series of mesoporous graphitic carbon nitride (MCN) nanometer materials, loaded onto the reduced graphene oxide aerogel (rGOA) with macroscopic three-dimensional (3D) porous structure, were prepared using reduction self-assembly method. The composite aerogel of MCN/rGOA hybrid (MCN/GO mass ratio of 3:9) showed the highest adsorption rate of 73.7% for removing rhodamine b (RhB) solution of 20 mg L^{-1}, whereas the total effect of adsorption and visible-light catalysis reached 95.2% within 80 min. Meanwhile, the material also showed good stability, and the removal rate was still about 89% after repeating the experiments for five times. The material characterization was carried out using various techniques, which indicated that hybrid aerogels were successfully combined. The specific surface increases from 18 m^2/g of MCN to 149 m^2/g for MCN/rGOA hybrid. The hybrid aerogel not only has good adsorption effect, but also exhibits adequate photocatalysis. The composite firstly interacts with the RhB through π–π adsorption, and then, the photocatalysis is improved by increasing the electron transfer efficiency and inhibiting the electron–hole recombination for good conductivity. Through scavenger experiments, it is shown that h^+ free radicals are the dominant oxidizer during photocatalytic degradation.

Address correspondence to E-mail: jwang1@bjtu.edu.cn

https://doi.org/10.1007/s10853-019-03531-7

Introduction

Nowadays, environmental pollution and energy shortage have become the two major worldwide problems. The solution to the problem of water pollution under the premise of energy conservation has attracted extensive attention [1, 2]. With the rapid development of industry, especially in the developing countries, the annual production of organic dyes has reached 7×10^5 tons, which is widely used in paper making, leather processing, textile dyeing, cosmetics, and pharmaceutical manufacturing industries [2–6]. Organic dye has become one of the important pollution sources for aquatic environment. At present, the methods to solve the pollution problem of organic dyes include biodegradation, physics and chemical adsorption, advanced oxidation, and visible-light catalysis [6]. Visible-light catalysis not only saves energy, but also degrades organic pollutants, due to which, it has attracted more and more attention [7].

As a new generation of metal-free semiconductor material, graphitic carbon nitride (g-C_3N_4) has received more and more attention in the field of visible-light catalysis since its first use by Wang et al. in 2009 [8, 9]. Compared with the traditional photocatalytic materials, g-C_3N_4 exhibits easy preparation, wide range of precursors (melamine, dicyandiamide, urea, and thiourea) with extensive preparation of resources in the earth, appealing electronic band structure, tunable band gaps of width (1.8–2.7 eV), high physical and chemical stability, non-toxicity, non-polluting, responsiveness to visible light (within 460–698 nm, it can utilize 13–49% solar energy). Graphitic carbon nitride is widely applied in the field of catalysis (photocatalytic water cracking for hydrogen production, photocatalytic reduction of carbon dioxide for hydrocarbon fuel, photocatalytic degradation of pollutants and disinfection of bacteria, and reduction of heavy metals) [7, 10, 11]. It also has some disadvantages, such as small specific surface area, low light energy utilization, and serious electron–hole recombination [12]. In order to solve these issues, researchers have developed various nanostructures (such as nanosheets, nanoparticles, and nanorods) [13–15], constructed heterogeneous junctions with other semiconductor materials [16, 17], and modified g-C_3N_4 using metal nanoparticles or carbon nanomaterials [18, 19]. Bai et al. prepared porous S-g-C_3N_4/MoS_2, which increased the specific surface area and enhanced the photocatalytic activity [20]. However, the nanometer photocatalytic powder limited the light mass transfer and was difficult to be reclaimed in its actual use.

As a new carbon material, three-dimensional (3D) self-assembly of pure graphene sheet materials was reported in 2010 [21]. It has attracted more and more attention of researchers due to its characteristics of large specific surface, low density, high elasticity, and strong adsorption. Reduced graphene oxide aerogels not only provide the attachment site for powder photocatalytic materials, but also have good adsorption capacity [22–25]. In addition, good conductivity can improve the electron transfer efficiency and can effectively inhibit the electron–hole synthesis. Meng et al. had successfully prepared reduced graphene oxide aerogel electrode materials with larger surface area using SiO_2 composite graphene oxide [26]. Compared to two-dimensional (2D) graphene, it is easy to recycle and reuse [27]. In addition, three-dimensional (3D) reduced graphene oxide aerogel can also regulate the shape, size, and density of aerogel by controlling the concentration of graphene oxide and the shape of the reactor [28]. Zhang et al. successfully combined molybdenum disulfide (MoS_2) and aerogel to improve the transfer rate of electrons and reuse [29]. Therefore, integrating the advantages of photocatalysis and reduced graphene aerogel, the combination of composite aerogel can not only improve the catalytic efficiency of visible light, but can also be recycled and reused, which makes it more suitable for practical engineering applications.

Tang et al. greatly improved the degradation efficiency of dyes through composite preparation of nanosheet g-C_3N_4 using grapheme [30]. He et al. used nanoscale g-C_3N_4, carbon quantum dots and graphene aerogel ternary compound to degrade the dye wastewater [28]. Compared with the traditional g-C_3N_4, mesoporous g-C_3N_4 has a porous structure, and the folded plane structure makes the mesoporous g-C_3N_4 have a larger specific surface area, which is more conducive to the adsorption of pollutants [9]. Compared with the nanosheet g-C_3N_4, the preparation of mesoporous g-C_3N_4 is simpler and is better suited to practical engineering applications [31]. However, reports on the characteristics and performance of hybrid aerogel of mesoporous g-C_3N_4 and rGOA are scarce in the literature. In this work, 3D mesoporous MCN/rGOA hybrid metal-free adsorbent and visible-light catalyst was fabricated.

The advantages of mesoporous g-C_3N_4 and rGOA with enhanced adsorption and photocatalytic activity were explored. In order to detect the microstructure, optical properties and macroscopic morphologies of the samples were characterized using X-ray diffraction, X-ray photoelectron spectroscopy, Fourier-transform infrared spectroscopy, N_2 adsorption–desorption, diffuse reflectance UV–Vis diffuse reflectance spectra, and photoluminescence emission spectroscopy. Through the degradation of RhB, the separation and transmission mechanism of electron–holes was revealed.

Experimental

Materials

Potassium permanganate ($KMnO_4$), concentrated sulfuric acid (H_2SO_4, 98%), hydrogen peroxide (H_2O_2, 30%), and hydrochloric acid (HCl, 37%) were obtained from Sinopharm Chemical Reagent Co., Ltd., China. Flaky graphite powder was obtained from Yu Kai graphite powder, China. Furthermore, sodium bisulfite ($NaHSO_3$) was purchased from Tianjin Yongda Chemical Reagent Co., Ltd., China. Melamine ($C_3H_6N_6$), ammonium oxalate (AO), ascorbic acid (AA), and isopropyl alcohol (IPA) were purchased from Aladdin Industrial Co., Ltd., China. All the reagents used in the experiments were of analytical grade and used without further purification. Deionized water was used in all the experiments.

Preparation of mesoporous graphitic carbon nitride (MCN)

Mesoporous graphitic carbon nitride (MCN) was prepared using thermal condensation of melamine as described in a previous work [9]. In a typical process, melamine was first added to hot deionized water. After cooling down, the appropriate amount of hydrochloric acid (HCl, 37%) was slowly added to the above melamine solution. Then, a magnetic stirrer was used to stir the solution for 30 min. The mixture was vacuum-dried under 80 °C to obtain melamine hydrochloride. Then, melamine hydrochloride was stored in a crucible with a cover and heated to 500 °C in a muffle furnace for 2 h with the heating rate of 20 °C min^{-1}, followed by heating at the rate of 4 °C min^{-1} to 520 °C for 2 h. After cooling and grinding, yellowish mesoporous g-C_3N_4 was obtained.

Preparation of graphene oxide (GO)

Graphene oxide (GO) was prepared from flaky graphite powder using a modified Hummers' method [32]. Firstly, 2 g of flaky graphite powder was oxidized using 50 mL concentrated sulfuric acid (H_2SO_4, 98%) and stirred for 1 h in an ice bath, which kept below 4 °C. Secondly, 6 g of $KMnO_4$ was slowly added to the mixture with vigorous agitation for 30 min and the temperature was controlled so that it did not to exceed 10 °C. Thirdly, the mixture was heated to 35 °C for 1 h. Then, 90 mL of deionized water was added to the mixture, heated to 98 °C, and maintained at this temperature for 30 min. Finally, 100 mL of deionized water was added to form GO mixture. In order to reduce the residual permanganate and manganese dioxide, the solution was treated with 20 mL H_2O_2 (30%) and stirred for 0.5 h until no obvious bubbles appeared. At last, the mixture was washed using deionized water to a pH of 4–6.

Synthesis of composite MCN and reduced graphene oxide aerogels (rGOA)

A series of GO with different concentrations (1.5, 2.0, 2.5, 3.0, 3.5 mg mL^{-1}) was optimized to prepare rGOA for adsorbing RhB. Composite MCN/rGOA hybrid was prepared using a previously reported aerogel preparation method [33]. Firstly, a certain mass of MCN was added to ultra-pure water and treated using ultrasound for 140 min. Secondly, the optimum GO concentration and 512 mg of $NaHSO_3$ were added to MCN water solution. The solution was sonicated for 20 min. Then, it was put into the drum wind drying oven (DHG-9030A, China) and heated for 2.5 h under 95 °C. Finally, the mixture was rinsed using deionized water to remove impurities and freeze-dried. Different mass proportions of MCN/rGOA hybrids were prepared (MCN/GO = 6:9, MCN/GO = 5:9, MCN/GO = 4:9, MCN/GO = 3:9, MCN/GO = 2:9). Scheme 1 illustrates the fabrication scheme and the corresponding digital photograph of the 3D mesoporous MCN/rGOA hybrids.

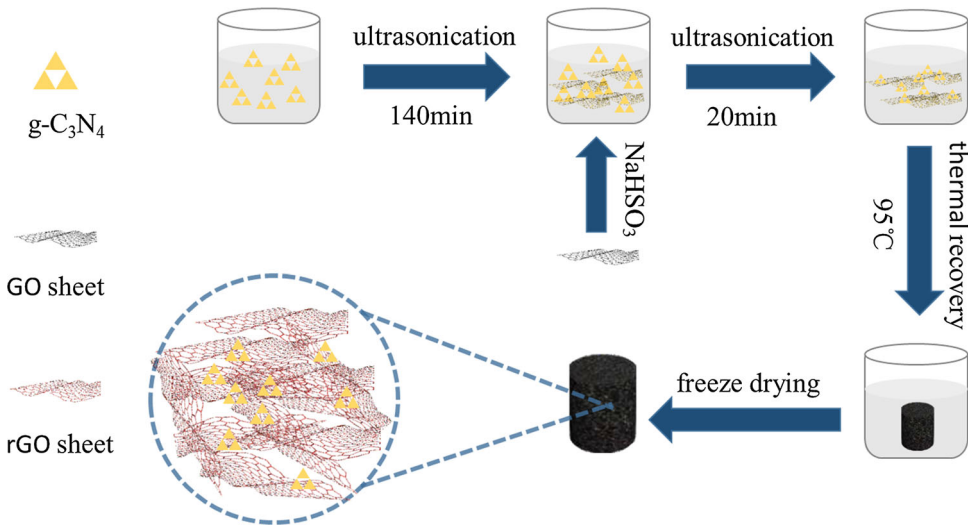

Scheme 1 Preparation scheme of MCN/rGOA hybrids.

Characterization

The samples were characterized using X-ray diffraction (XRD, Bruker D8-Advance, USA), transmission electron microscope (TEM), and high-resolution transmission electron microscopy (HRTEM, JEM-2100F, Japan), scanning electronic microscopy (SEM, JSM-7800F), X-ray photoelectron spectroscopy (XPS, Thermo, Escalab 250xi, USA), Fourier-transform infrared spectroscopy (FTIR, PerkinElmer Spectrum GX), diffuse reflectance UV–Vis diffuse reflectance spectra (DRS, Agilent, Cary 5000, USA), N_2 adsorption–desorption (Micrometrics ASAP2020, USA), and photoluminescence (PL, F-4600 FL, Hitachi, Japan) emission spectroscopy.

Adsorption and photocatalytic activity

The properties of samples were evaluated using adsorption and degradation of RhB at room temperature. The prepared samples and RhB solution (20 mg L^{-1}, 100 mL) were added to a 250-mL glass container to directly show the adsorption performance of the sample under dark conditions. The glass container was placed under a 300-W xenon lamp, which filtered out the light below 420 nm to show the adsorption and photodegradation capacity of the sample. Then, 3 mL of the solution was taken at the intervals of 20 min, and the solution concentration was measured using an ultraviolet visible spectrophotometer (Beijing Purkinje General Instrument Co., Ltd., China) at 551 nm. The removal rate was assessed using C/C_0 and the rate constant (k, min^{-1}).

$$\ln\frac{C}{C_0} = kt \tag{1}$$

where C_0 solution initial concentration (20 mg L^{-1}), C solution concentration at the corresponding time, mg L^{-1}, and t degradation time, min.

The procedure for the visible-light catalysis experiments was same as the above process. After each experiment, the composite aerogels were taken out and desorbed in anhydrous ethanol for 1.5 h. Then, the anhydrous ethanol was removed by soaking in deionized water for 30 min. The samples were freeze-dried for recycling. The above photocatalytic experiment was recycled five times to test the stability of the sample.

Results and discussion

Morphology and structure of as-prepared hybrid

The macroscopic morphology and mechanical properties of photocatalytic materials are shown in Fig. 1. Figure 1a shows the shape and size of the composite aerogels. The MCN/rGOA hybrid (3:9) was pressed with a weight of 160 g. After removing the weight, they restored to their original shape without any damage. Therefore, the mechanical stability of the reduced graphene oxide aerogel was very good, as shown in Fig. 1b, c.

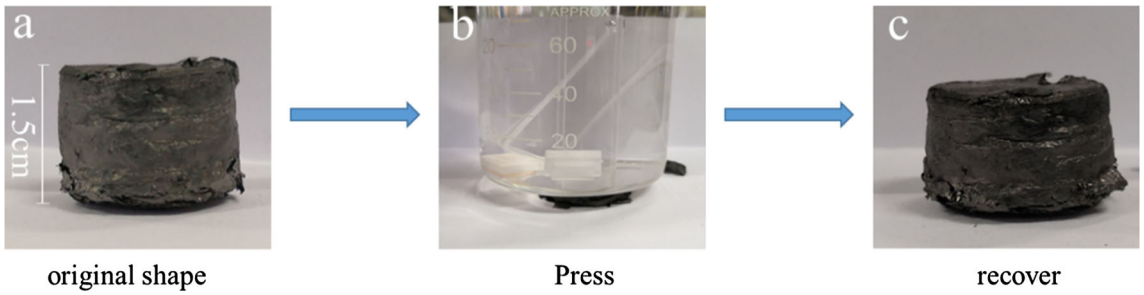

Figure 1 **a** Digital image of the as-prepared MCN/rGOA hybrid (3:9), **b**, **c** mechanical properties of the hybrid aerogels.

The SEM images of MCN, rGOA, MCN/rGOA composites are shown in Fig. 2a–d. The MCN morphology is shown in Fig. 2d, while the nanosheet layer and porous structure can also be seen clearly. rGOA can be observed from Fig. 2a, b, which shows that its structure was composed of two-dimensional (2D) flaky rGO that was self-assembled and stacked at high temperature to form three-dimensional porous structure. The 3D layered structure can improve the transmission efficiency of electrons and effectively inhibit the combination of electrons and holes, thus improving the efficiency of visible-light catalysis. In addition, rGO 2D sheet structure provided attachment points for MCN, due to which, it can be firmly attached. This can also be observed from the SEM image of the composite aerogels shown in Fig. 2c. There were scaly protrusions in the rGOA layer, indicating that the 2D flaky MCN adheres to rGOA.

The transmission electron microscope images of rGOA, MCN/rGOA composite are shown in Fig. 3. The porous structure of MCN can be seen in Fig. 3a, and the flaky structure of rGO is shown in Fig. 3b. As illustrated in Fig. 3c, MCN is distributed on the layer of rGO without damaging the layered porous structure of rGOA. The 2D lamellar MCN was firmly attached to the graphene sheet, indicating that MCN and rGO can be well combined. In Fig. 3d, lattice fringes of MCN prepared with melamine that was treated with hydrochloric acid were not observed. However, it is noticed that the stacking distance of 0.324 nm from the interlayer-stacking of the conjugated aromatic system corresponding to (002) plane belongs to the lattice distance of MCN observed in Fig. 3f. Tang et al. and Yan et al. reported that the

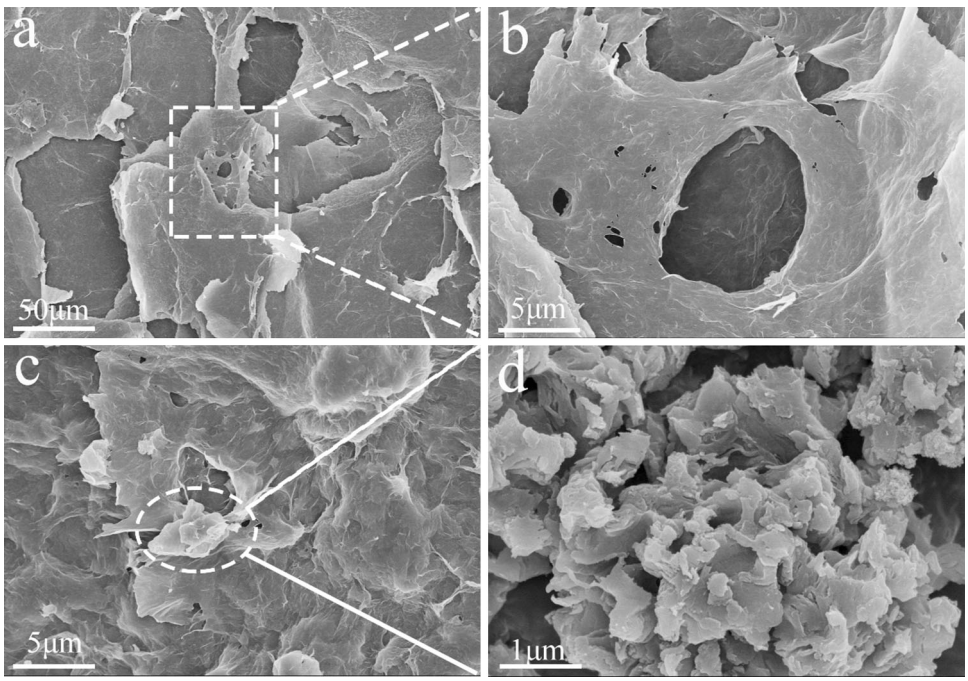

Figure 2 FESEM images of **a**, **b** rGOA, **c** MCN/rGOA hybrid (3:9), **d** MCN.

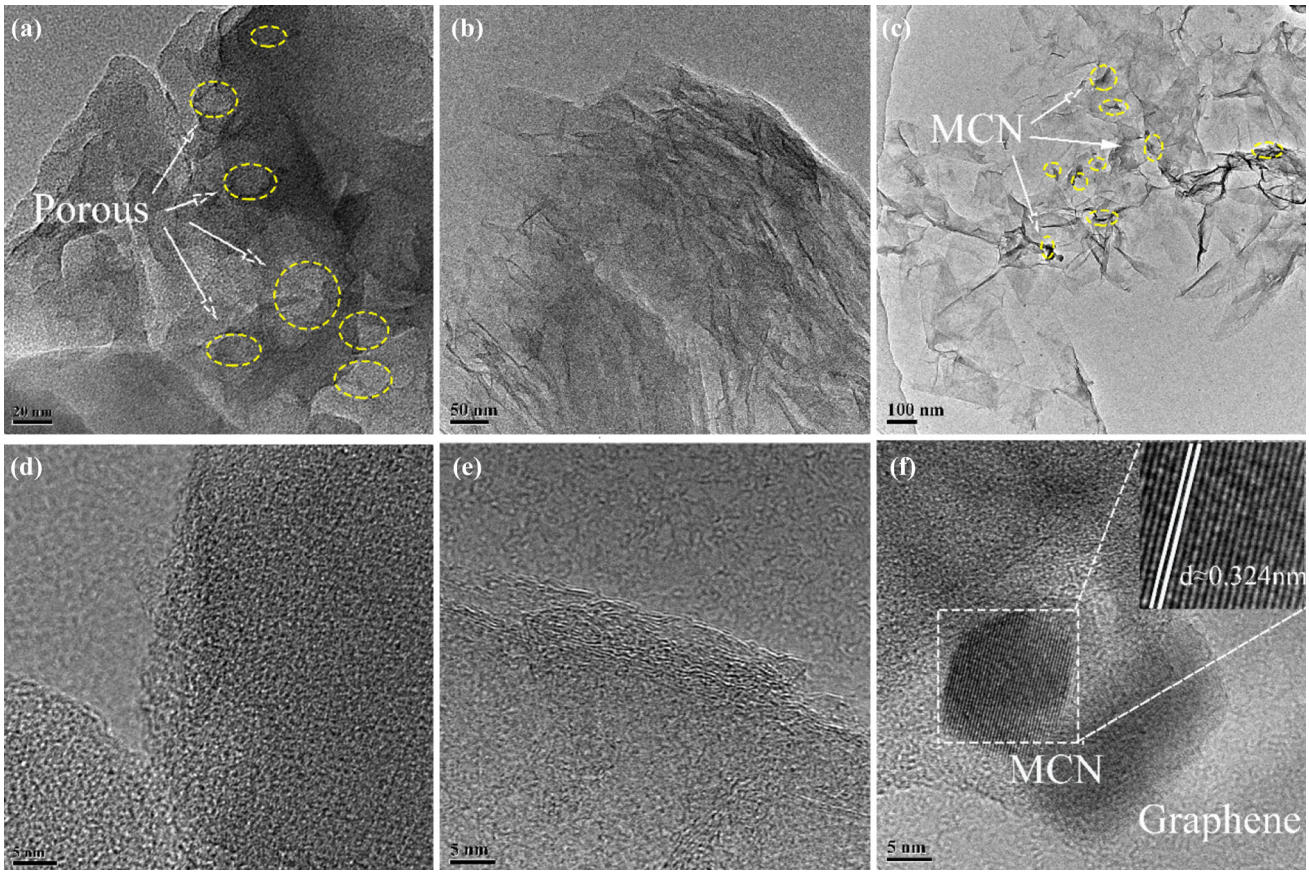

Figure 3 TEM image of **a** MCN, **b** rGOA, **c** MCN/rGOA hybrid (3:9), HRTEM images of **d** MCN, **e** rGOA, **f** MCN/rGOA hybrid (3:9).

stack spacing of 002 crystal plane of g-C_3N_4 was 0.324 nm (for sulfonated g-C_3N_4 composite graphene aerogel) and 0.337 nm (for Cu_2O and g-C_3N_4 composite aerogel) using HRTEM [30, 34]. In the HRTEM of composite aerogels, it can be seen that its layered porous structure is consistent with the rGOA structure.

As shown in Fig. 4, the crystal structure characteristics of MCN, rGOA and MCN/rGOA composite were analyzed using X-ray diffraction (XRD). MCN exhibited two obvious diffraction peaks at 13.1° and 27.2°, among which the weak diffraction peak corresponded to MCN in the structure of (100) crystal plane with the repeated in-plane cycle, whereas the strong diffraction peak corresponded to conjugate layers stacked (002) crystal plane diffraction peak [34]. Besides, the existence of (100) crystal plane indicated the plane connection rule of triazine unit in g-C_3N_4. Single-phase rGOA at 22.6° indicated a wide diffraction peak, highlighting that the material is a loose accumulation (002) crystal plane [35]. Stack distance in MCN-conjugated aromatic system is

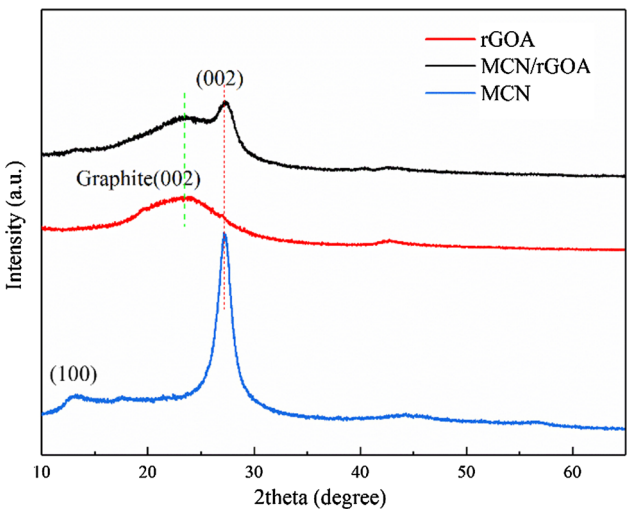

Figure 4 XRD patterns of the prepared photocatalysts.

observed from the HRTEM (Fig. 3f). The diffraction peak of MCN at 13.1° in MCN/rGOA hybrids disappeared, indicating that the MCN crystal structure in the process of composite has changed. It might be that GO has a thermal coupling between the MCN

layers and rGO nanosheets during the hydrothermal reaction [28]. Furthermore, the diffraction peak at 27.2° shows that the composite is successfully realized.

The molecular structure of the samples is analyzed using Fourier-transform infrared (FTIR) spectra, as shown in Fig. 5. An anti-symmetric characteristic absorption peak of rGOA at 1120 cm^{-1} represents the stretching vibration of C–O–C bond in rGOA [36], and the stretching vibration peak of –OH at 3300–3500 cm^{-1} [37]. The anti-symmetric characteristic absorption peak at 1200–1650 cm^{-1} is the stretching vibration of MCN's typical heterocyclic structure. The anti-symmetric characteristic peak of the stretching vibration of g-C_3N_4's special triazine structure appeared at 805 cm^{-1} [38], while N–H bond and H_2O stretching vibration appeared at 3000–3500 cm^{-1} [39]. Compared with the pure MCN and rGOA, MCN/rGOA composites presented the above characteristic peaks and showed obvious changes in the abovementioned bands, indicating that MCN has been successfully combined into rGOA and formed a new bond with rGOA. In this way, it could improve the electron transfer efficiency and the photocatalytic efficiency of MCN.

In order to further analyze the components of samples, XPS was used to characterize the elements and structures of the samples. The results are shown in Fig. 6. From the full spectrum of XPS, it can be seen that rGOA contains only C and O elements, while in the composite aerogel, there were N elements (besides the original C and O elements of rGOA). In order to further analyze the combined states of C, N, and O, the three elements were subjected to peak fitting. As shown in Fig. 6b, rGOA exhibited characteristic peaks at 284.2 eV and 285.4 eV in the C1*s* spectrum, which correspond to the binding state of C in the graphitic carbon (C–C) and C–O in rGOA, respectively. Compared with the rGOA, the characteristic peak at 288.0 eV in the composite aerogels corresponds to the binding state of N–C =N bonds in the sp^2 C in MCN. According to the O1*s* figure, both the pure rGOA and rGOA combined with MCN showed two 530.9 eV characteristic peaks, which correspond to C–O in rGOA, while the characteristic peaks of H_2O at 531.6 eV are due to the absorption of water present in air [28]. In the N1 s Fig. 6c, there were no N elements in rGOA. Two characteristic peaks of 398.3 eV and 400.3 eV were found in the composite aerogels, which correspond to C–N=C and N–$(C)_3$, respectively [40]. The existence of C–N=C bond indicates that a new bond was formed between MCN and rGOA, which enabled MCN to better attach to rGOA, and improved the transmission efficiency of photoelectrons and the efficiency of catalysis.

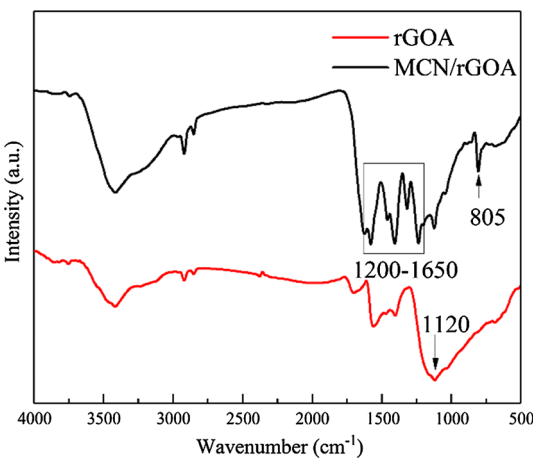

Figure 5 FTIR spectra of the prepared photocatalysts.

In order to verify more structural properties (specific surface area and pore size) of the material, nitrogen adsorption–desorption experiments were carried out, as shown in Fig. 7. In nitrogen adsorption–desorption isothermal curves shown in Fig. 7a, it can be seen that MCN, rGOA, and MCN/rGOA hybrids had great hysteresis loop, which according to the IUPAC belonged to type IV adsorption desorption isotherm, and is caused by the porous structure existing in the sample. Therefore, the three samples showed relatively poor nitrogen adsorption characteristics at P/P_0 = 0.45–1.00, and the hysteretic circulations indicated the existence of pores, thus demonstrating the porosity of MCN. In Fig. 7b, it was observed that the pore size of MCN was mainly distributed at 2–50 nm, with a small number of medium and large holes. The pore size of rGOA was 2–5 nm, while that of MCN/rGOA hybrid was 2–8 nm, indicating that the composite material retained the original porous structure, which was also confirmed by the pore size distribution. The specific surface area and the pore volumes of the samples are listed in Table 1. Compared with the rGOA, the BJH observed average pore diameter in the MCN/rGOA composite was improved.

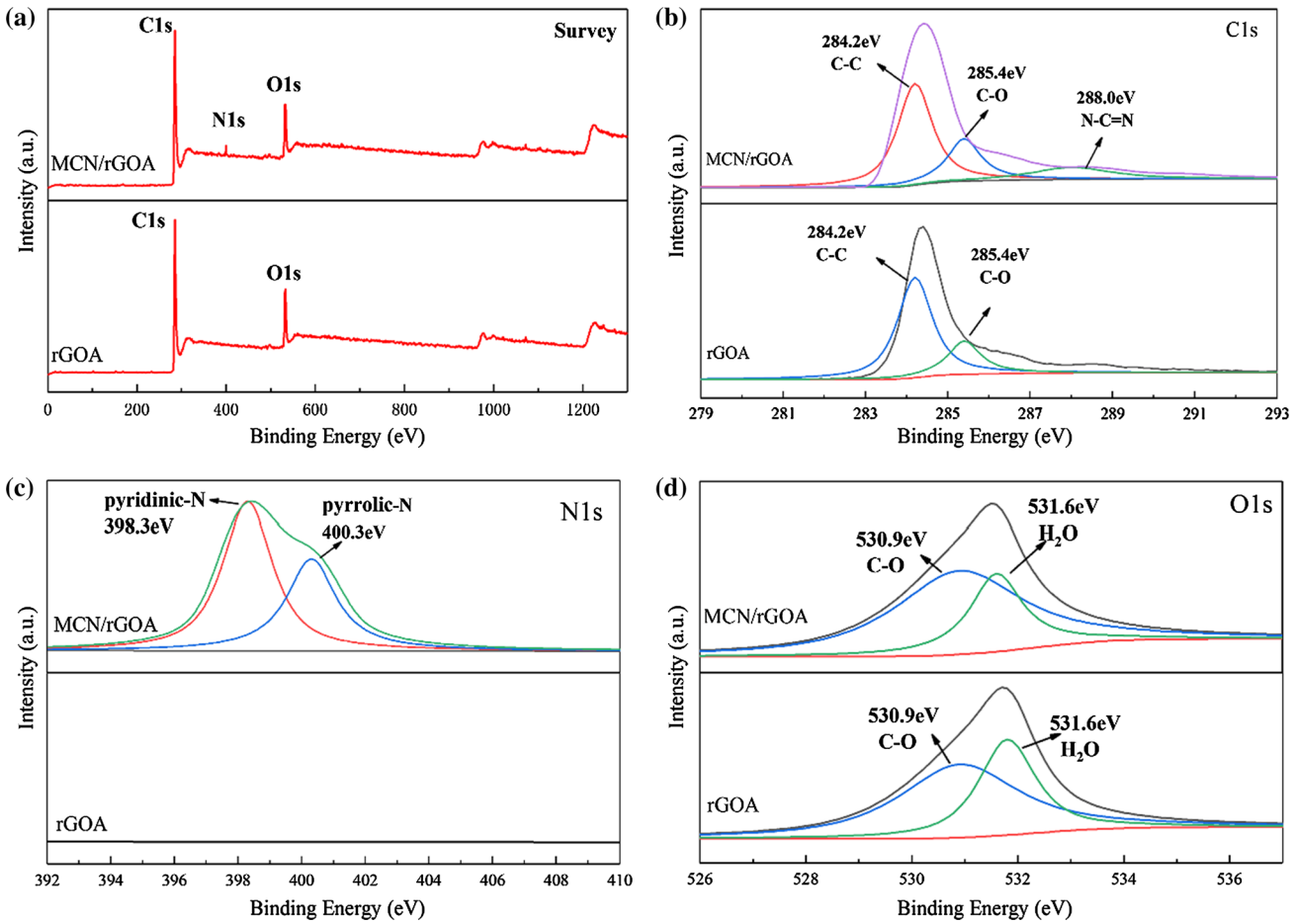

Figure 6 XPS spectra of rGOA and MCN/rGOA hybrid (3:9), **a** Survey, **b** N1s, **c** C1s, **d** O1s.

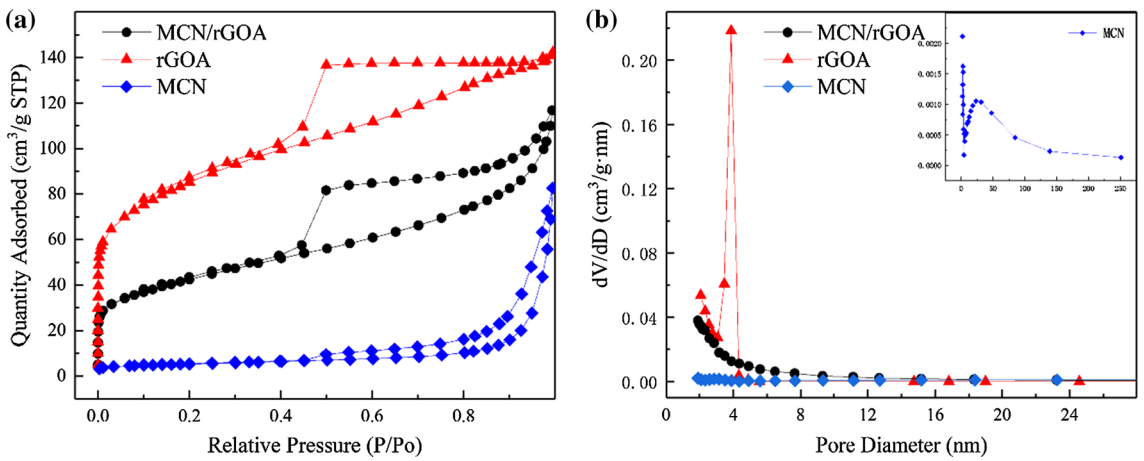

Figure 7 **a** N_2 adsorption–desorption isotherms for MCN, rGOA, MCN/rGOA hybrid (3:9), respectively, **b** BJH pore-size distributions for MCN, rGOA, MCN/rGOA hybrid (3:9).

Optical properties of the hybrid

Macroscopic 3D porous framework might affect the optical properties of composite aerogels. For this reason, the optical properties of UV–Vis DRS were characterized and are shown in Fig. 8. It can be seen that all the samples can absorb visible light. At < 480 nm, pure MCN shows the intrinsic absorption

Table 1 Information about the framework of MCN, rGOA, and MCN/rGOA hybrid

Sample	S^{a}_{BET} (m^2 g^{-1})	V^{b}_{p} (cm^3 g^{-1})	D^{c}_{a} (nm)	D^{d}_{a} (nm)	D^{e}_{a} (nm)
MCN	18.06	0.13	28.33	32.80	18.96
rGOA	294.97	0.22	2.98	3.54	3.32
MCN/rGOA	149.37	0.18	4.84	5.83	4.89

[a]S_{BET} BET surface area

[b]V_p Single point adsorption total pore volume

[c]D_a Adsorption average pore width (4 V/A by BET)

[d]D_a BJH adsorption average pore diameter (4 V/A)

[e]D_a BJH desorption average pore diameter (4 V/A)

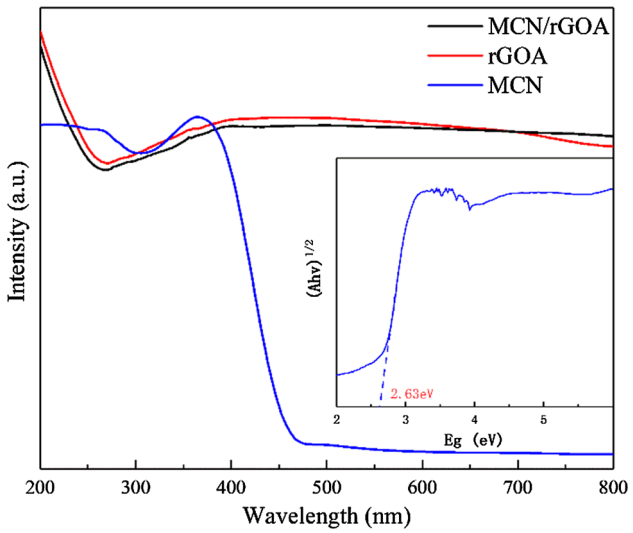

Figure 8 Optical properties of MCN, rGOA, and MCN/rGOA hybrid (3:9) determined using UV–Vis DRS.

of g-C_3N_4. At < 384 nm, the absorption of visible light is stronger than that of rGOA and MCN complexes, though the absorption intensity of visible light between 384 and 800 nm is much weaker than that of MCN on rGOA. The absorption of light in the whole band of rGOA may be caused by repeated refraction of light in the porous structure of rGOA [34, 41]. The photonic absorption coefficient—photonic energy curve was obtained using the DRS curve, and the band gap value of MCN was found to be 2.63 eV based upon the tangent method. The above analysis showed that a stronger and wider range of light absorption is very beneficial to the photocatalysis of composite aerogels.

In the process of photocatalytic reaction, the photogenerated electron–hole pairs are one of the important factors affecting the photocatalytic performance. In order to further verify the efficiency of photogenerated electron–hole separation, fluorescence characteristics of the samples were determined and are shown in Fig. 9. MCN has a strong fluorescence emission peak at 470 nm, which is the intrinsic fluorescence emission peak, derived from MCN powder (namely the electron transition of the valence band to the conduction band), and the fluorescence generated by the composite of holes, which is consistent with the results of DRS [12]. When rGOA and MCN were combined, the intensity of the fluorescence emission peak was greatly reduced and the fluorescence emission peak appeared at 487 nm. The reduction of peak strength and red shift indicate that the reduced graphene oxide aerogel improved the transfer efficiency of photogenerated electrons, thus effectively inhibiting the combination of electrons and holes. It was observed that PL peak red-shift through loaded MCN, and the signal moved toward a longer wavelength [42]. In short, it not only enhances the

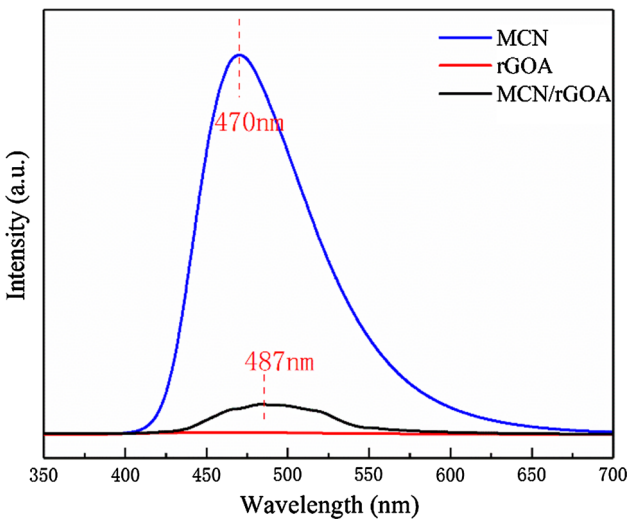

Figure 9 Optical properties of MCN, rGOA, and MCN/rGOA hybrid (3:9) determined using PL.

absorption range of light, but also inhibits the recombination of light-induced vectors, which proves that rGOA is a good photocatalytic carrier.

Visible-light-driven catalytic performance

Before synthesizing the composite aerogels, rGOA with different concentrations of GO was prepared, and the adsorption performance of RhB was optimized, as shown in Fig. 10. Within 240 min, 3.0 mg mL^{-1} of rGOA adsorption performance was the best, which reached 89% adsorption. For different concentrations of GO, aerogels density and aperture were different. As the concentration increases, its density gradually increases. When the concentration was 3.0 mg mL^{-1}, the effect was the best. However, when the concentration was higher than 3.0 mg mL^{-1}, the pore size might be smaller, which was not conducive to adsorption, and therefore, the adsorption efficiency decreased.

In order to evaluate the performance of reduced graphene oxide aerogel supported MCN photocatalyst in practical applications, the organic dye wastewater, simulated using RhB, was adsorbed and degraded through photocatalysis under visible light. The blank test showed that the concentration of RhB did not change significantly under dark or visible-light irradiation. From Fig. 11a, it can be seen that, under the dark conditions, pure MCN and composite aerogels loaded with different masses of MCN had different adsorption capacities. The best adsorption capacity was observed for the MCN/rGOA hybrid

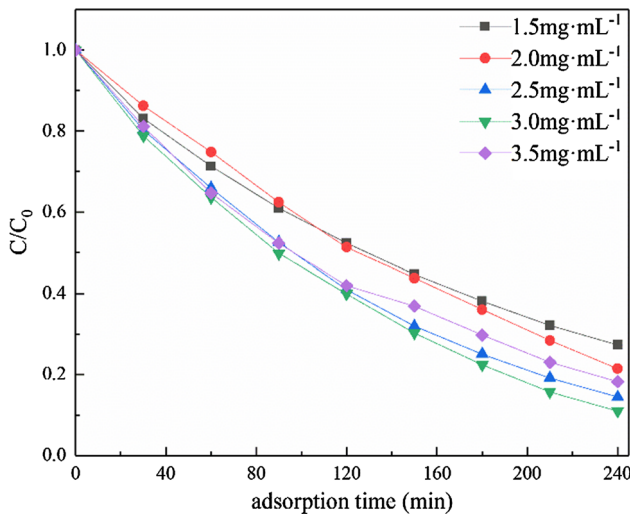

Figure 10 Adsorption capacity of the as-prepared rGOA on RhB aqueous solutions.

(3:9), which reached 73.6% in 80 min, while the worst adsorption was observed for MCN, which reached the value of 9%. The poor adsorption performance of MCN could be due to smaller surface area, which offers fewer adsorption sites. The adsorption capacity of rGOA is much higher than that of pure MCN due to its unique three-dimensional porous frame structure and large specific surface area. In addition, the selective adsorption of aromatic dyes was carried out by electron coupling. The adsorption rate with the loaded amount of 5:9 was 73.6%, while the adsorption rate of rGOA was 49%, indicating that the addition of MCN changed the structural properties of rGOA and was conducive to improving the adsorption capacity. Before the addition of g-C_3N_4, rGOA has the lower density and floats on the surface of water. The addition of MCN increases the density of rGOA. The composite aerogel is suspended in liquid, and more parts are impregnated in the solution than that of rGOA, making the composite aerogel have a better contact with RhB molecules in the solution. Meanwhile, the addition of MCN also changes the porous structure of rGOA, as shown in Fig. 7 and Table 1. The pore size of composite aerogels becomes larger, which is more conducive for RhB to enter the macroscopic aerogels and adhere to the surface of rGO sheets.

The ability of the samples' adsorption and photocatalytic degradation for RhB was tested under the condition of visible-light irradiation. As can be seen from Fig. 11b, the degradation rate of MCN/rGOA hybrid (3:9) for RhB was 95.2% within 80 min, while that of pure MCN was 65.5%, which increased by 29.7%. According to the characterization of BET, the larger specific surface area of MCN/rGOA composite is better for the adsorption of organic dyes. The unique porous structure is more advantageous for harvesting the light, thus improving the photocatalytic efficiency. Meanwhile, due to its light weight, the hybrid photocatalyst can remain suspended on the surface of the target water medium and easily absorb visible light. In addition, the reduced graphene oxide aerogel loaded with MCN could produce more electron hole pairs, and the combination of electron holes was reduced, which improved the efficiency of visible-light catalysis. However, with the increase of MCN's content, the degradation rate became slow, and the removal of MCN/rGOA hybrid (6:9) was found to be only around 59%. This phenomenon may be due to the increase of MCN

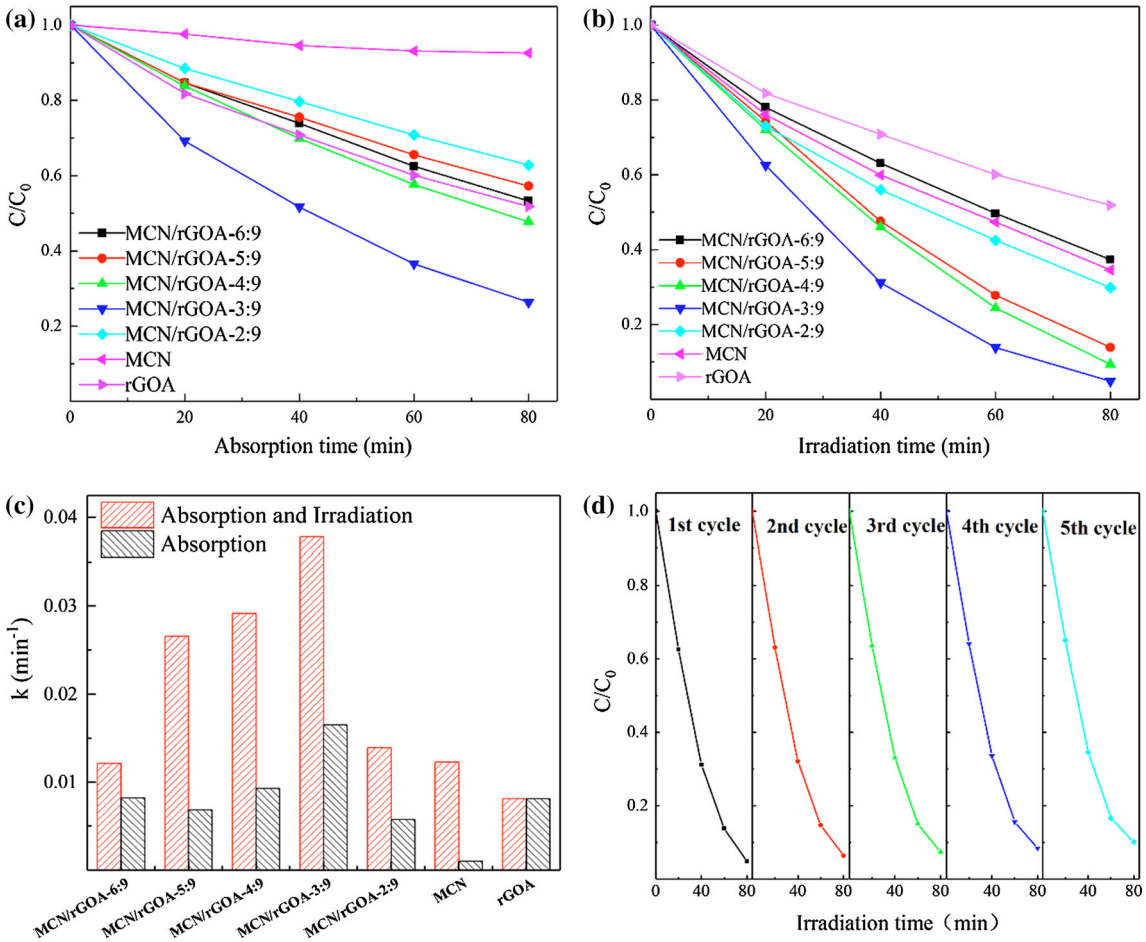

Figure 11 RhB removal performance of MCN, rGOA, and MCN/rGOA hybrids **a** Adsorption, **b** adsorption and visible-light-driven photocatalytic degradation, **c** adsorption and photocatalytic degradation kinetic constants, **d** stability of the MCN/rGOA hybrids.

content, due to which the density of the composite aerogels becomes larger, resulting in the reduction of utilization of light. In addition, the increase in MCN changed the porous structure of the composite aerogels, thus reducing the adsorption contact area as well as the visible-light contact. The degradation rate of organic dyes can also be controlled by controlling the loading capacity of MCN.

The rate constants of the samples are shown in Fig. 11c. It could be seen that the rate constant of MCN loaded by reduced graphene oxide aerogel was significantly higher than that of pure MCN. The rate constants of MCN/rGOA hybrid (3:9) and MCN were 0.03781 min^{-1} and 0.0123 min^{-1}, respectively, indicating that the rate constant of composite aerogel was 3.07 times higher than that of MCN. This suggests that the resulting composite was better suited to removing RhB. At the same time, the k of adsorption–photodegradation is greater than the adsorption amount of the investigated materials, which proved that the generated materials had obvious visible-light-driven photocatalytic activity for the degradation of RhB in wastewater.

Moreover, the photocatalytic stability is another important factor to be considered for photocatalysts. Therefore, the stability test was carried out on the MCN/rGOA hybrid (3:9). The experimental results of the sample are shown in Fig. 11d. The removal efficiency of RhB was still around 89% after recycling for five times, indicating that the sample had good stability.

Proposed photocatalytic mechanisms

Through photocatalytic degradation of RhB, it was found that the composite aerogels had a good ability to remove organic dyes in water. In order to further understand its degradation mechanism, a free radical

capture experiment was conducted. Isopropanol, ammonium oxalate, and ascorbic acid were used to capture ·OH, h^+, and $\cdot O_2^-$, respectively. As illustrated in Fig. 12, the scavenger effect during the degradations of RhB was observed. It was also observed that, compared with the controlled experiment, all the scavengers were inhibited. The RhB degradation was significantly inhibited in a solution containing ammonium oxalate, followed by a weak inhibition in the solution containing isopropyl alcohol and ascorbic acid. The experiment of free radical capture shows that h^+ is the main active substance. The effect decreased after adding isopropanol, possibly due to the reason that isopropanol inhibited the adsorption capacity of aerogel on RhB.

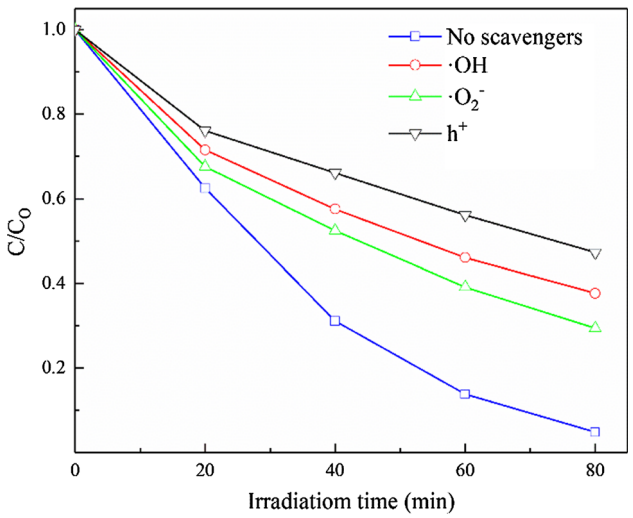

Figure 12 Effect of scavengers on RhB's degradation for MCN/rGOA hybrid (3:9) under visible-light irradiation.

It is well known that the energy band structure of photocatalytic materials was directly related to the separation efficiency of electron–hole pairs. According to empirical correlation (Eqs. (2), (3)), the edge potential between the conduction band and valence band of photocatalytic semiconductor materials can be deduced:

$$E_{VB} = \chi - E_e + 0.5E_g \quad (2)$$

$$E_{CB} = E_{VB} - E_g \quad (3)$$

where E_{VB} valence band-edge potentials, eV, E_{CB} conduction band-edge potentials, eV, E_g the band gap energy of semiconductor, eV, E_e the energy of free electrons, which is about 4.5 eV on the hydrogen scale, eV, and χ the Mulliken electronegativity of a semiconductor oxide, where $\chi_{g\text{-}C3N4}$ = 4.72 eV.

According to the calculations, the E_{VB} and E_{CB} edge potentials of MCN are 1.54 eV and − 1.09 eV, whereas E_{VB} = 1.54 eV, due to which it becomes difficult to oxidize OH^{-1} to ·OH ($E_{OH-/\cdot OH}$ = + 1.99 eV, $E_{H2O/\cdot OH}$ = 2.40 eV). When irradiated by visible light, MCN produced more electrons, which were immediately transferred onto rGOA. Due to this reason, more holes were left on the valence band and were consumed to oxidize the dye. Furthermore, E_{CB} = − 1.09 eV can reduce O_2 to $\cdot O_2^-$ ($E_{O2/\cdot\bar{O}2}$ = − 0.33 eV). On the basis of the above results, a tentative mechanism for the enhanced photocatalytic performance of MCN/rGOA hybrids was proposed, which is illustrated in Scheme 2.

Scheme 2 Mechanism of MCN/rGOA hybrid (3:9).

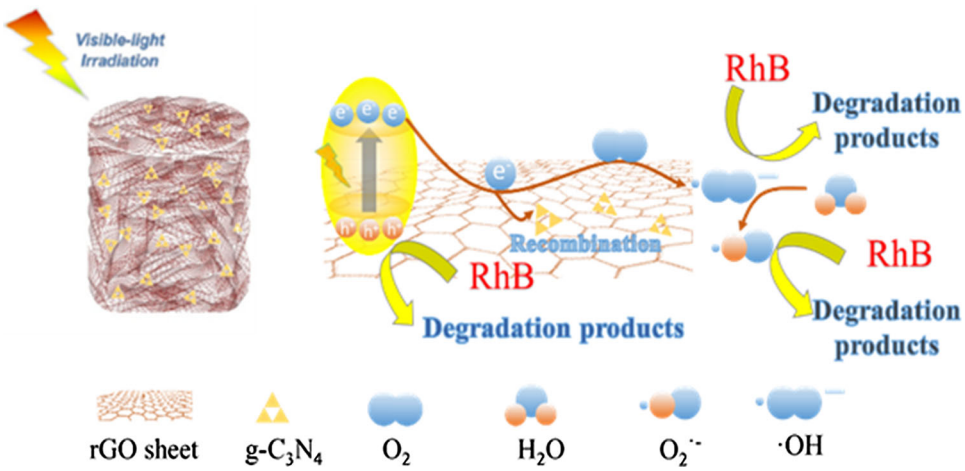

$$\mathrm{MCN} + \mathrm{rGOA} + h\nu = \mathrm{e}^- + \mathrm{h}^+ \quad (4)$$

$$\mathrm{O_2} + \mathrm{e}^- = \cdot\mathrm{O_2^-} \quad (5)$$

$$\mathrm{H_2O/O_2^{\cdot -}} = \cdot\mathrm{OH} \quad (6)$$

Therefore, the composite aerogels showed good removal effect for RhB, which is attributed to two aspects. On the one hand, the larger specific surface area of reduced graphene oxide aerogel provided more active sites for dye adsorption, and the aromatic dyes were selected through electron coupling. The unique porous structure was more favorable for transferring the light in the carrier, due to which the photocatalytic activity was improved more effectively in the photocatalytic process. On the other hand, the combination of MCN and rGO enabled the rapid transfer of electrons on the carrier and improved the separation of electron–hole pairs, due to which the photocatalytic capacity was enhanced.

Conclusions

In this work, the composite hydrogels were prepared by one-step reduction self-assembly method. The macroporous aerogels were obtained by freeze-drying. Various characterization methods showed that MCN and rGO were well combined. Compared with the conventional MCN in the visible-light catalytic experiment, MCN/rGOA hybrid (3:9) not only showed good photocatalytic effect in removing RhB, but also possessed excellent adsorption capacity. After five cycles of experiments, the removal effect could still reach about 89%, due to which MCN/rGOA hybrid (3:9) showed good stability. The rGO sheet quickly transferred the photoelectrons, leaving lots of holes to oxidize the pollutant, thus suggesting that the high specific surface area and good conductivity of rGOA make it a good carrier for photocatalytic materials. Therefore, the composite aerogels loaded with MCN are good materials in the field of organic dye degradation catalyzed by visible light.

Acknowledgements

This work was supported by the State Key Laboratory of Environmental Chemistry and Ecotoxicology, the Research Center for Eco-Environmental Sciences, the Chinese Academy of Sciences, the Beijing Key Laboratory of Aqueous Typical Pollutants Control and Water Quality Safeguard and the Beijing Key Laboratory of Aqueous Typical Pollutants Control and Water Quality Safeguard. The authors wish to thank Prof. Jing Chuanyong, Associate Professor Yan Wei and Yan Li for their guidance to analyze the photocatalytic mechanism. This research did not receive any specific grant from public, commercial, or not-for-profit funding agencies.

References

[1] Yin S, Han J, Zhou T, Xu R (2015) Recent progress in g-C_3N_4 based low cost photocatalytic system: activity enhancement and emerging applications. Catal Sci Technol 5:548–561. https://doi.org/10.1039/c5cy00938c

[2] Liang Z, Zhao Z, Sun T, Shi W, Cui F (2017) Enhanced adsorption of the cationic dyes in the spherical CuO/mesosilica nano composite and impact of solution chemistry. J Colloid Interfaces Sci 485:192–200. https://doi.org/10.1016/j.jcis.2016.09.028

[3] He K, Chen G, Zeng G, Chen A, Huang Z, Shi J, Huang T, Peng M, Hu L (2018) Three-dimensional graphene supported catalysts for organic dyes degradation. Appl Catal B Environ 228:19–28. https://doi.org/10.1016/j.apcatb.2018.01.061

[4] Liu Q, Shen J, Yang X, Zhang T, Tang H (2018) 3D reduced graphene oxide aerogel-mediated Z-scheme photocatalytic system for highly efficient solar-driven water oxidation and removal of antibiotics. Appl Catal B Environ 232:562–573. https://doi.org/10.1016/j.apcatb.2018.03.100

[5] Zhang J, Qi P, Li J, Zheng X, Liu P, Guan X, Zheng G (2018) Three-dimensional Fe_2O_3–TiO_2–graphene aerogel nanocomposites with enhanced adsorption and visible light-driven photocatalytic performance in the removal of RhB dyes. J Ind Eng Chem 61:407–415. https://doi.org/10.1016/j.jiec.2017.12.040

[6] Chen Z, Ma J, Yang K, Feng S, Tan W, Tao Y, Mao H, Kong Y (2017) Preparation of S-doped TiO_2—three dimensional graphene aerogels as a highly efficient photocatalyst. Synth Met 231:51–57. https://doi.org/10.1016/j.synthmet.2017.06.020

[7] Ding F, Yang D, Tong Z, Nan Y, Wang Y, Zou X, Jiang Z (2017) Graphitic carbon nitride-based nanocomposites as visible-light driven photocatalysts for environmental purification. Environ Sci Nano 4:1455–1469. https://doi.org/10.1039/c7en00255f

[8] Wen J, Xie J, Chen X, Li X (2017) A review on g-C_3N_4-based photocatalysts. Appl Surf Sci 391:72–123. https://doi.org/10.1016/j.apsusc.2016.07.030

[9] Dong G, Zhang L (2012) Porous structure dependent photoreactivity of graphitic carbon nitride under visible light. J Mater Chem 22:1160–1166. https://doi.org/10.1039/C1JM14312C

[10] Ong W, Tan L, Ng YH, Yong S, Chai S (2016) Graphitic carbon nitride ($g\text{-}C_3N_4$)-based photocatalysts for artificial photosynthesis and environmental remediation: are we a step closer to achieving sustainability? Chem Rev 116:7159–7329. https://doi.org/10.1021/acs.chemrev.6b00075

[11] Zheng Q, Durkin DP, Elenewski JE, Sun Y, Banek NA, Hua L, Chen H, Wagner MJ, Zhang W, Shuai D (2016) Visible-light-responsive graphitic carbon nitride: rational design and photocatalytic applications for water treatment. Environ Sci Technol 50:12938–12948. https://doi.org/10.1021/acs.est.6b02579

[12] Liang Q, Li Z, Yu X, Huang Z, Kang F, Yang Q (2015) Macroscopic 3D porous graphitic carbon nitride monolith for enhanced photocatalytic hydrogen evolution. Adv Mater 27:4634–4639. https://doi.org/10.1002/adma.201502057

[13] Yang L, Liu X, Liu Z, Wang C, Liu G, Li Q, Feng X (2018) Enhanced photocatalytic activity of $g\text{-}C_3N_4$ 2D nanosheets through thermal exfoliation using dicyandiamide as precursor. Ceram Int. https://doi.org/10.1016/j.ceramint.2018.06.105

[14] Wang H, Liang Y, Liu L, Hu J, Cui W (2018) Highly ordered TiO_2 nanotube arrays wrapped with $g\text{-}C_3N_4$ nanoparticles for efficient charge separation and increased photoelectrocatalytic degradation of phenol. J Hazard Mater 344:369–380. https://doi.org/10.1016/j.jhazmat.2017.10.044

[15] Tahir B, Tahir M, Amin NAS (2017) Photo-induced CO_2 reduction by CH_4/H_2O to fuels over Cu-modified $g\text{-}C_3N_4$ nanorods under simulated solar energy. Appl Surf Sci 419:875–885. https://doi.org/10.1016/j.apsusc.2017.05.117

[16] Li Y, Chen Z, Wang M, Zhang L, Bao S (2018) Interface engineered construction of porous $g\text{-}C_3N_4/TiO_2$ heterostructure for enhanced photocatalysis of organic pollutants. Appl Surf Sci 440:229–236. https://doi.org/10.1016/j.apsusc.2018.01.106

[17] Mishra A, Mehta A, Kainth S, Basu S (2018) Effect of $g\text{-}C_3N_4$ loading on TiO_2/bentonite nanocomposites for efficient heterogeneous photocatalytic degradation of industrial dye under visible light. J Alloys Compd 764:406–415. https://doi.org/10.1016/j.jallcom.2018.06.089

[18] Zou J, Wang L, Luo J, Nie Y, Xing Q, Luo X, Du H, Luo S, Suib SL (2016) Synthesis and efficient visible light photocatalytic H_2 evolution of a metal-free $g\text{-}C_3N_4$/-graphene quantum dots hybrid photocatalyst. Appl Catal B Environ 193:103–109. https://doi.org/10.1016/j.apcatb.2016.04.017

[19] Nagajyothi PC, Pandurangan M, Vattikuti SVP, Tettey CO, Sreekanth TVM, Shim J (2017) Enhanced photocatalytic activity of $Ag/g\text{-}C_3N_4$ composite. Sep Purif Technol 188:228–237. https://doi.org/10.1016/j.seppur.2017.07.026

[20] Bai J, Lv W, Ni Z, Wang Z, Chen G, Xu H, Qin H, Zheng Z, Li X (2018) Integrating MoS_2 on sulfur-doped porous $g\text{-}C_3N_4$ iostype heterojunction hybrids enhances visible-light photocatalytic performance. J Alloys Compd 768:766–774. https://doi.org/10.1016/j.jallcom.2018.07.286

[21] Xu Y, Sheng K, Li C, Shi G (2010) Self-assembled graphene hydrogelvia a one-step hydrothermal process. ACS Nano 4:4324–4330. https://doi.org/10.1021/nn101187z

[22] Chen F, Li S, Chen Q, Zheng X, Liu P, Fang S (2018) 3D graphene aerogels-supported Ag and $Ag@Ag_3PO_4$ heterostructure for the efficient adsorption-photocatalysis capture of different dye pollutants in water. Mater Res Bull 105:334–341. https://doi.org/10.1016/j.materresbull.2018.05.013

[23] Lu K, Yuan L, Xin X, Xu Y (2018) Hybridization of graphene oxide with commercial graphene for constructing 3D metal-free aerogel with enhanced photocatalysis. Appl Catal B Environ 226:16–22. https://doi.org/10.1016/j.apcatb.2017.12.032

[24] Shu D, Feng F, Han H, Ma Z (2017) Prominent adsorption performance of amino-functionalized ultra-light graphene aerogel for methyl orange and amaranth. Chem Eng J 324:1–9. https://doi.org/10.1016/j.cej.2017.04.136

[25] Lu X, Mao Q, Chen Y, Bao L, Tong L, Xiong Q, Qin H, Pan H, Ji Z (2018) A novel oxygen vacancy introduced microstructural reconstruction of SnO_2–graphene nanocomposite: demonstration of enhanced electrochemical performance for sodium storage. Electrochim Acta 282:351–361. https://doi.org/10.1016/j.electacta.2018.06.069

[26] Meng J, Cao Y, Suo Y, Liu Y, Zhang J, Zheng X (2015) Facile fabrication of 3D SiO_2@graphene aerogel composites as anode material for lithium ion batteries. Electrochim Acta 176:1001–1009. https://doi.org/10.1016/j.electacta.2015.07.141

[27] Fan Y, Ma W, Han D, Gan S, Dong X, Niu L (2015) Convenient recycling of 3D Ag*X*/graphene aerogels (*X* = Br, Cl) for efficient photocatalytic degradation of water pollutants. Adv Mater 27:3767–3773. https://doi.org/10.1002/adma.201500391

[28] He H, Huang L, Zhong Z, Tan S (2018) Constructing three-dimensional porous graphene–carbon quantum dots/$g\text{-}C_3N_4$ nanosheet aerogel metal-free photocatalyst with enhanced photocatalytic activity. Appl Surf Sci 441:285–294. https://doi.org/10.1016/j.apsusc.2018.01.298

[29] Zhang R, Wan W, Li D (2017) Three-dimensional MoS_2/reduced graphene oxide aerogel as a macroscopic visible-

light photocatalyst. Chin J Catal. https://doi.org/10.1016/s1872

[30] Tang L, Jia C, Xue Y, Li L, Wang A, Xu G, Liu N, Wu M (2017) Fabrication of compressible and recyclable macroscopic g-C_3N_4/GO aerogel hybrids for visible-light harvesting: a promising strategy for water remediation. Appl Catal B 219:241–248. https://doi.org/10.1016/j.apcatb.2017.07.053

[31] Dong F, Li Y, Wang Z, Ho W (2015) Enhanced visible light photocatalytic activity and oxidation ability of porous graphene-like g-C_3N_4 nanosheets via thermal exfoliation. Appl Surf Sci 358:393–403. https://doi.org/10.1016/j.apsusc.2015.04.034

[32] Chen J, Yao B, Li C, Shi G (2013) An improved Hummers method for eco-friendly synthesis of graphene oxide. Carbon 64:225–229. https://doi.org/10.1016/j.carbon.2013.07.055

[33] Hu H, Zhao Z, Wan W, Gogotsi Y, Qiu J (2013) Ultralight and highly compressible graphene aerogels. Adv Mater 25:2219–2223. https://doi.org/10.1002/adma.201204530

[34] Yan X, Xu R, Guo J, Cai X, Chen D, Huang L, Xiong Y, Tan S (2017) Enhanced photocatalytic activity of Cu_2O/g-C_3N_4 heterojunction coupled with reduced graphene oxide three-dimensional aerogel photocatalysis. Mater Res Bull 96:18–27. https://doi.org/10.1016/j.materresbull.2016.12.009

[35] Zhou J, Ma L, Song H, Wu B, Chen X (2011) Durable high-rate performance of CuO hollow nanoparticles/graphene-nanosheet composite anode material for lithium-ion batteries. Electrochem Commun 13:1357–1360. https://doi.org/10.1016/j.elecom.2011.08.011

[36] Feng K, Tang B, Wu P (2014) Sulfonated graphene oxide–silica for highly selective Nafion-based proton exchange membranes. J Mater Chem A 2:16083–16092. https://doi.org/10.1039/C4TA03207A

[37] Wan W, Yu S, Dong F, Zhang Q, Zhou Y (2016) Efficient C_3N_4/graphene oxide aerogel macroscopic visible-light photocatalyst. J Mater Chem A 4:7823–7829

[38] Duan J, Chen S, Jaroniec M, Qiao SZ (2015) Porous C_3N_4 nanolayers@N-graphene films as catalyst electrodes for highly efficient hydrogen evolution. ACS Nano 9:931–940. https://doi.org/10.1021/nn506701x

[39] Chang B, Fu J, Chang B, Tian Y, Xi F, Dong X (2013) Novel C_3N_4–CdS composite photocatalysts with organic-inorganic heterojunctions: in suit synthesis, exceptional activity, high stability and photocatalytic mechanism. J Mater Chem A 1:3083–3090

[40] Hou Y, Wen Z, Cui S, Feng X, Chen J (2016) Strongly coupled ternary hybrid aerogels of N-deficient porous graphitic-C_3N_4 nanosheets/N-doped graphene/NiFe-layered double hydroxide for solar-driven photoelectrochemical water oxidation. Nano Lett 16:2268–2277. https://doi.org/10.1021/acs.nanolett.5b04496

[41] Cai J, Liu W, Li Z (2015) One-pot self-assembly of Cu_2O/RGO composite aerogel for aqueous photocatalysis. Appl Surf Sci 358:146–151. https://doi.org/10.1016/j.apsusc.2015.08.021

[42] Zhang X, Chi Z, Xu B, Chen C, Zhou X, Zhang Y, Liu S, Xu J (2012) End-group effects of piezofluorochromic aggregation-induced enhanced emission compounds containing distyrylanthracene. J Mater Chem 22:18505. https://doi.org/10.1039/c2jm33140c